WPJET1-PR(17) 17734

A Lasa et al.

ERO Modeling and Sensitivity Analysis of Erosion Enhanced by Magnetically Connected Antennas

Preprint of Paper to be submitted for publication in
Nuclear Fusion

This work has been carried out within the framework of the EUROfusion Consortium and has received funding from the Euratom research and training programme 2014-2018 under grant agreement No 633053. The views and opinions expressed herein do not necessarily reflect those of the European Commission.

ERO Modeling and Sensitivity Analysis of Erosion Enhanced by Magnetically Connected Antennas

A. Lasa[1], D. Borodin[2], J.M. Canik[1], C.C. Klepper[1], M. Groth[3], A. Kirschner[2], M.I Airila[4], I. Borodkina[5], R. Ding[6] and JET Contributors*

EUROfusion Consortium, JET, Culham Science Center, Abingdon, OX14 3DB, UK
[1] Oak Ridge National Laboratory, Oak Ridge, TN 37831-6169, USA
[2] Forschungszentrum Jülich GmbH, Institut für Energie- und Klimaforschung - Plasmaphysik, Partner of the Trilateral Euregio Cluster (TEC), 52425 Jülich, Germany
[3] Aalto University, P.O.Box 14100, FIN-00076 Aalto, Finland
[4] VTT Technical Research Centre of Finland, P.O.Box 1000, FIN-02044 VTT, Finland
[5] National Research Nuclear University (Mephi), Kashirskoe sh., 31, Moscow, Russia
[6] General Atomics, General Atomics, San Diego, CA, US

E-mail: lasaesquisaa@ornl.gov

Abstract.

Experiments at JET showed enhanced, asymmetric beryllium (Be) erosion at outer wall limiters when magnetically connected ICRH antennas were in operation. A first modeling effort using the ERO code reproduced qualitatively the experimental outcome. However, local plasma parameters − in particular when 3D distributions are of interest − can be difficult to determine from available diagnostics and so erosion / impurity transport modeling input relies on output from other codes and simplified models, increasing uncertainties in the outcome. In the present contribution, we introduce and evaluate the impact of improved models, as well as further parameters with largest uncertainties, on erosion and emission simulated by ERO: (i) The magnetic geometry, which defines both the LCFS position (thus the background plasma profiles) and connection lengths between components, the latter leading to shadowing of ion fluxes, has been revised; (ii) Anomalous motion of ionized impurities, defined by the perpendicular diffusion coefficient, has been revisited; (iii) Erosion yields that account for energy and angular distributions of background plasma ions under the present oblique magnetic field configuration and enhanced sheath potential, have been introduced; (iv) The effect of additional erosion sources, such as charge-exchange neutral fluxes, which are dominant in recessed areas like antennas, has been evaluated; (v) Chemically assisted release of Be in molecular form has been included. The

*See the author list of "Overview of the JET results in support to ITER" by X. Litaudon *et al.* to be published in Nucl. Fusion Special issue: overview and summary reports from the 26th FEC (Kyoto, Japan, 17-22 Oct 2016)

sensitivity analysis highlights a qualitative effect (i.e., change in emission patterns) of magnetic shadowing, anomalous diffusion, and inclusion of neutral fluxes and molecular release of Be. The LCFS location, and energy and angular distribution of background plasma fluxes impact erosion quantitatively. ERO simulations including all features described above match experimentally measured Be I and Be II signals. However, increases in erosion with variation of ICRH antenna's RF power are not fully captured by ERO's emission measurements, as most contributions from plasma wetted surfaces fall outside the volume observed by sightlines.

1. Introduction

Plasma surface interactions (PSI) may lead to a wide range of plasma facing component degrading effects, such as surface erosion, consequent re- or co-deposition with fuel and plasma contamination. In the main wall of a tokamak, which in the JET ITER-Like Wall (JET-ILW) is made of beryllium (Be), PSIs are most intense on limiter surfaces. Further, use of RF antennas has been linked with enhanced erosion of plasma facing components, such as in recently observed increase in Be erosion of outer-wall limiters (OWL) of JET when ion-cyclotron resonant heating (ICRH) antennas were used [1]. Analysis of these experiments concluded that enhanced and asymmetric Be emission was observed when the magnetically connected antenna was switched on, compared to when any other or no antennas were used: 2-3 times higher emission was measured by the sightline pointing at the neighboring antenna, compared to that looking at the limiter side. Both sightlines observed a factor of 2-3 higher emission with antenna toggling. Increases in surface erosion were attributed to perturbations in the sheath caused by the electric field of the magnetically connected antenna [2].

Surface erosion and consequent localized impurity production, resulting from RF-sheath formations (via magnetic connection) at locations distant from the powered antenna have been long predicted [3], although experimental observations of such localized sources have been scarce. For instance, using poloidally-resolved spectroscopic measurements of both a neutral tungsten line (W I) and deuterium Balmer-alpha (D_α) on the lateral protection limiters of two, toroidally-separated antennas, the effective yield for W sputtering was estimated in ASDEX-Upgrade (AUG) [4]. By alternate powering of each of the antennas, poloidally asymmetric, RF sheath-enhanced W sources were shown and thus characterized for both local and remote (by magnetic connection) manifestation of these effects. Another important outcome of this AUG study was that it clearly documented RF sheath-induced erosion on the leading edge of the limiter (for both the local and the remote antenna) as opposed to the recessed antenna structures, including the straps and Faraday screen. Also, in an earlier study on Alcator C-mod, an observed toroidal asymmetry in the erosion of the boronization layer (on the top of the outboard divertor) was used, specifically during ICRH heated plasmas, to show that the locally-enhanced erosion regions could be traced back to the active ICRH antenna along

magnetic fieldlines [5]. A similar effect was suspected to be a potential source of the increased W plasma content when ICRH is on in JET-ILW [6]. However, such ICRH-enhanced W sources in JET have so far not been located during dedicated discharges [6] and the search for such (still) missing sources has continued in the background of more recent JET-ILW experiments. Thus, in the JET case addressed here, this ability to directly detect enhanced, edge Be line emission at limiter locations magnetically connected to distant ICRH antennas in an ILW environment, coupled with substantial recent improvements in the determination of sputter yield coefficients for Be specific to this same environment [7, 8, 9], provides a unique opportunity to quantify this erosion process. Furthermore, the fact that ITER will operate with ICRH antennas in similar wall environment, makes this study of great interest, in particular in terms of the impact of this localized erosion on the lifetime of water-cooled Be PFCs.

A first effort to model enhanced Be erosion by ICRH antennas in the JET-ILW was performed using the ERO code, where the sheath rectification was represented by an additional biasing voltage [10]. The modeling outcome was in qualitative agreement with experiments: a 2-3 fold in Be erosion was observed with increasing biasing and the Be II emission asymmetry was reproduced.

However, not all parameters used in modeling of surface erosion and impurity transport can be determined experimentally or calculated from first principles. Therefore, these values are provided by other codes or simplified models, increasing uncertainties in the input and thus, output (erosion, emission, re-deposition, etc.). Sensitivity tests of these 'estimates' allow gaining insight on the processes involved, evaluate the impact of each process in the output and help finding sets of values that best reproduce experiments. This exercise also allows to identify key fields where advances would reduce uncertainties most, improving future modeling and gaining confidence in predictive capabilities.

In the present study, simplified models implemented in ERO have been revisited for inputs more consistent with assumptions made when reconstructing the background plasma, and to account in greater detail for the surface description provided by materials' modeling codes. Further physical processes estimated to impact erosion have also been implemented. Sensitivity tests over these models have allowed to evaluate their effect and validity. The same approach has also been applied to testing input parameters with largest uncertainties in the initial ERO study of enhanced Be erosion [10]. For instance, the accuracy of the magnetic configuration has been revisited by looking at the position of the separatrix, as well as connection lengths that vary across the surface. The latter parameter directly relates the perpendicular diffusion coefficient and magnetic shadowing of the density (i.e., faster decay in areas of shorter connection length) [11, 12]. Background plasma ion impact energy and angles, which determine the sputtering yield, are also affected by the magnetic configuration and related sheath structure. Energy and angular distributions calculated analytically for the present geometry have been

introduced in ERO for better estimates of gross erosion. Further, the impact of adding further erosion sources, such as fluxes of neutrals energized through charge-exchange processes, has been evaluated. This process is estimated to be the dominant source in shadowed (i.e., not plasma exposed) surfaces, such as the all-Be Faraday shields of the studied JET (type-"A2") antennas [13], which are radially out from the tangency point of the OWL's. Finally, we evaluated the impact of molecular processes in the model used for Be erosion.

The manuscript is structured as follows: the set-up of experiments, ERO simulations and the case used as reference for sensitivity tests, are described in Section 2. The implementation and effect of each parameter tested, and model introduced or improved, are presented in Section 3.1. The combined effect of all features and exploration of the complete model for comparison with experiments, are discussed in Section 3.2. Finally, the main outcome of this work is summarized and steps towards reducing uncertainties in future impurity modeling are suggested.

2. Method

2.1. Experiments

Two L-mode pulses were run at JET to study enhanced Be erosion due to magnetically connected ICRH antennas. Beryllium emission near the OWL located to the left − looking from the surface towards the plasma center − of JET antenna-D was monitored: Be II (467.4 nm) during JET pulse number (JPN) 81172 and Be I (457.3 nm) in JPN-81173. Two sightlines were used to observe Be emission: D14 pointing to the neighboring antenna side of the limiter, and D12 looking at the limiter side away from antenna D. In each plasma pulse, three antennas were switched ON-and-OFF, one at a time: antenna-D, adjacent or 'neighboring' to the monitored limiter; antenna-C, magnetically connected to the limiter, also referred to as 'remote antenna' in what follows; and antenna 'A+B', located 'far' from the limiter, preventing any interaction with it. Further experimental details, such as limiter and antennas' location and geometry, have been described by Klepper *et al.* in Refs. [1, 10].

2.2. ERO modeling

The 3D Monte Carlo code ERO [14] has been used in the present exercise. This ERO version was first built for modeling of ITER blanket modules [15], then modified and extensively used to study erosion of JET inner-wall limiters [7] and recently further adjusted to include the outer wall mid-plane geometry [10]. Here, we build on the latter ERO version by targeting most uncertain input parameters and introducing a number of physical effects which, although relevant for the case in hand, were earlier neglected.

In ERO simulations, impurities eroded by the background plasma are followed until leaving the simulated volume or deposited on the surface. Particles eroded by the traced impurities are not followed in the present case. This is well justified by the negligible re-deposition of and re-erosion by traced particles in comparison to the primary erosion source: a background plasma representative of L-mode discharges, composed mainly of D ions and with a low Be concentration. The simulated volume was of $900 \times 620 \times 230\text{mm}^3$ in the toroidal, poloidal and radial direction, respectively, including an OWL and part of the neighboring antenna D (Fig.1). The surface is divided into a grid of 100×50 points in the toroidal and poloidal direction, respectively. Synthetic diagnostics included three sightlines: two (D12 and D14) located as in experiments (see Section 2.1) and an additional chord (D13) located in between, which was unused in JPN 81172-73 and therefore dismissed during our analysis. The geometry of each sightline was approximated by a cylinder of 35 mm in radius, which starts at the light collection optics port and ends where the sightline intercepts the limiter or antenna D's surface, with the thus projected spots being determined via backlighting of the optical path ahead of each experimental campaign. This spatial calibration of the sightlines is part of the standard procedure for JET's core charge exchange spectroscopy (CXRS) diagnostic, from whose sightlines were used for this experiment, as previously discussed [1, 10]. A 2D projection of the D12−D14 sighlines is plotted in all Be emission figures shown in this article, Figs. 3, 6 and 7 (only a line is shown for D13, as it is unused in our analysis). Background plasma parameters, i.e., electron density (n_e), electron temperature (T_e) and ion temperature (T_i) were provided by EDGE2D-Eirene simulations [16, 17]. These simulations were carried out for JPN 81472, which was run in a similar magnetic configuration as JPN 81172-73 (differences between these two pulses are discussed in Section 3.1.1). As the EDGE2D limiting surface is the lower outer baffle in JET, leaving a gap between the outermost grid cell and the walls surface, these profiles have been extrapolated to the ERO surface following an exponential decay. The method is described in detail in [18]. Two different scenarios were modeled by EDEGE2D-Eirene, assuming low and high recycling at the divertor (LR and HR, respectively). These assumptions lead to a 2-fold higher n_e and 1.5 times lower T_i in the latter case. The difference in T_e was negligible and an opposite flow direction was noticed. Only physical sputtering of Be is considered, although a fraction of the eroded Be can be emitted in molecular form (Section 3.1.6). The Eckstein 2007 model (Ref. [19], with corrections from [20]) was used to calculate the sputtering yields, both for erosion by the background plasma, as well as by traced particles. Ten computational particles are emitted from each surface cell − representing erosion by the background plasma − for all sensitivity tests (Section 3.1), and 100 particles/cell for simulations using the complete model and comparison to experiments (Section 3.2). Further details on the ERO version used, as well as the simulation set-up, are provided in Ref. [10] and references therein.

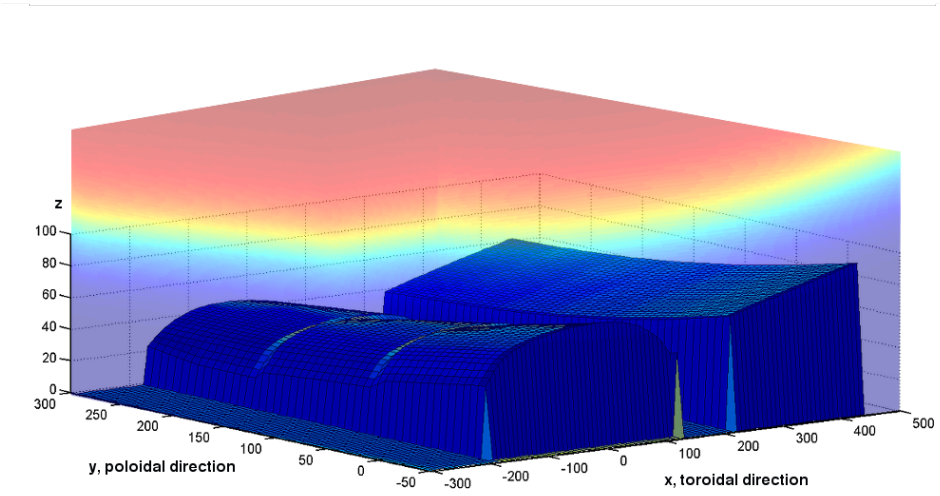

Figure 1: 3D image of the geometry used in ERO, including the outer wall limiter (front) and part of the neighboring antenna D (back) surface, with poloidal and toroidal electron density profiles overlaid, decaying from the LCFS (orange) towards the wall (blue). All spacial dimensions are given in [mm].

2.3. Reference case parameters

A reference case has been established to evaluate the impact of each added feature, in which: the last closed field surface was positioned according to the EFIT [21] reconstruction of the JPN modeled here (see Section 3.1.1); the perpendicular diffusion coefficient was calculated for a simple SOL model (Section 3.1.2); only surface areas with a connection length greater than 42m were assumed to be plasma-wetted (referred as 'crude shadowing model', Section 3.1.3); without erosion by charge-exchange neutral fluxes (introduced in Section 3.1.4); with surface erosion by the background plasma calculated for analytically derived impact energy and angular distributions for deuterium (D), but without additional biasing [22] (Section 3.1.5); and without molecular erosion of Be (Section 3.1.6). All cases analyzed in Section 3 assumed a LR background plasma, as the flow velocity lead to Be II emission patterns that matched better experimental findings [10]. Erosion yields obtained assuming 50% D concentration at the surface (ERO-Min) were used, which not only have shown to better match experiments [7, 9], but are also backed up by recent multi-scale Kinetic Monte Carlo − Molecular Dynamics modeling [23].

Every model extension introduced or input parameter scan performed in Section 3.1 is compared to the reference case described above. Thus, instead of absolute values, the relative impact of the model extension on the output is presented in Section 3.1, e.g., ratio of erosion in the extended:reference case (Figs. 2 and **??**), or erosion and emission pattern changes (Figs. 3 and 4).

3. Implementation, results and discussion

3.1. Extension of the model

3.1.1. Magnetic geometry Background plasma parameters, provided by EDGE2D-Eirene simulations, are extrapolated from the last closed field surface (LCFS) to the ERO surface following an exponential decay. Therefore, the magnetic field configuration, which defines the position of the LCFS and is here calculated by the EFIT reconstruction [21], sets the distance in which the exponential density and temperature decay are applied. Thus, small variations in the LCFS position ($\mathcal{O}$(mm)) can lead to large changes ($\gtrsim$ 2-fold) in density, temperature and thus flux to the wall.

For instance, a slight shift in equilibrium − given by the EFIT reconstruction − is found in the case modeled here (JPN 81172-73), compared with that used to reproduce the background plasma (JPN 81472): the LCFS was found to be 1 cm further from the wall in the former case. Therefore, background plasma parameters were extrapolated to the ERO surface accounting for the updated magnetic configuration.

Shifting the LCFS leads to 1.5-2 times lower density and temperature (evaluated on the surface), reducing erosion by a 5 fold (Fig. 2). These changes are only quantitative, as all plasma-wetted areas are located at similar distances from the LCFS, thus being subject to comparable changes in plasma conditions with shifting the separatrix location. Note that shifts in the magnetic configuration lead to similar lowering of erosion also in simulations run assuming a pure Be surface (EROMax), or using the background plasma reconstructed for a high-recycling scenario (HR). Further details regarding these cases (EROMax, HR-plasma) are discussed in Ref. [10].

3.1.2. Perpendicular diffusion coefficient Processes leading to anomalous motion of ions, i.e., perpendicular to magnetic flux surfaces, and not described by classical effects (e.g., drifts), can be largely averaged into one parameter: the perpendicular diffusion coefficient. Radial transport of impurities in the scrape-off layer is to-date poorly understood [24, 25, 26] − more poorly than radial transport of deuterons. Hence, to allow for radial transport of beryllium ions in these ERO simulations we assume three different values or models.

As discussed in Section 3.1.3, a simple SOL model [11, 12] is assumed in our study to implement spatially varying densities, for which the perpendicular diffusion coefficient is given by:

$$D_\perp = \frac{\lambda^2 c_s}{L_C}. \tag{1}$$

In the present case, the sum of electron and ion temperatures is $T_e + T_i \sim 25$ eV; the connection length is $L_C \sim 48$m and the density decay length is $\lambda \sim 14$mm, near the limiter tip surface. These conditions result in $D_\perp \sim 0.12$ m^2/s. Being a parameter used by EDGE2D-Eirene to reconstruct the background plasma, this approach estimates a

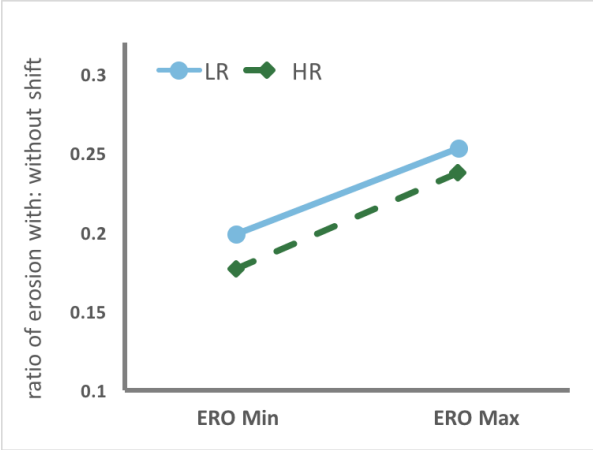

Figure 2: The total Be erosion calculated by ERO, with the background plasma provided by EDGE2D-Eirene and extrapolated to the surface assuming a 1 cm shift in the LCFS position (magnetic field configuration of JPN 81173), or without any shift (magnetic field configuration of JPN 81472). The output is expressed as the ratio of the two, $\text{erosion}_{JPN-81173} : \text{erosion}_{JPN-81472}$, (solid light blue line). For comparison, the same exercise is performed using a background plasma for the high-recycling scenario (HR, dashed dark green line). The ERO simulations assume a pure Be surface (ERO-max) or a Be surface with 50% D (ERO-min).

self-consistent $D_\perp$ value, based on local plasma parameters (T_e, T_i and λ). Indeed, in comparison to values used earlier in ERO or other models for $D_\perp$ (see paragraphs below), this value is in agreement with that used by the EDGE2D-Eirene simulations that provided the background plasma: 0.5 m^2/s at the separatrix and 1.0 m^2/s elsewhere [16]. It is also consistent with values suggested in the literature [11, 25], and calculated and used by other ERO studies [27, 28, 29].

ERO simulations using the perpendicular diffusion coefficient calculated for a simple SOL have been compared to runs using a negligible value of $D_\perp \sim 0.4$ mm^2/s, 6 orders of magnitude lower (used earlier in ERO [10]). Larger $D_\perp$ leads to small, yet non-zero re-deposition of traced Be ions ($\mathcal{O}(10^{13})$ atoms). However, the impact in Be II emission was negligible: patterns become 'noisier' with a higher $\text{D}_\perp$ (Figs. 3(a) and 3(b)), but with no quantitative change.

Finally, the Bohm diffusion coefficient, often assumed as upper boundary value for perpendicular diffusion, has also been tested:

$$D_{Bohm} = \frac{1}{16}\frac{k_B T}{eB}, \tag{2}$$

where B is the magnetic field strength. In the present case, $D_{Bohm} \sim 20$ m^2/s. Although only 2 orders of magnitude higher than $D_\perp$ for the simple SOL model − in comparison to the 6 order of magnitude difference discussed above − using the D_{Bohm} value in ERO

had a larger impact on the outcome: the total Be emission is lowered by a factor of 2 and the pattern is significantly more diffused (Fig. 3(c)) than in either case discussed above. Such difference can be understood in terms of the average perpendicular motion of an ion, $S_\perp = D_\perp \langle \tau_\perp \rangle$, where $\tau_\perp$ is the lifetime of an ionized particle in the ERO simulation, $\mathcal{O}(10^{-4}\text{s})$. For the former two values of $D_\perp$, the average perpendicular motion is much smaller than the system size: $\mathrm{D}_\perp = (4 \cdot 10^{-7} - 0.1\text{m}^2/\text{s}) \implies S_\perp \sim 10^{-5} - 10^{1}\text{mm}^2 \ll \text{cm}^2$. In contrast, the perpendicular motion assuming Bohms diffusion coefficient is comparable to the system size: $\mathrm{D}_\perp = D_{Bohm}$, $S_\perp \sim 10^3$ mm^2; and the effect of perpendicular diffusion is visible in the Be II emission pattern.

We conclude that the perpendicular diffusion coefficient can impact the outcome, mainly emission by and re-deposition of ionized particles. However, a significant effect is only expected for $\mathrm{D}_\perp$ values that lead to perpendicular motion ($S_\perp \sim D_\perp \langle \tau_\perp \rangle$) larger than the system size ($\mathcal{O}(\text{cm}^2)$). Under such condition, such as for D_{Bohm}, a higher perpendicular diffusion coefficient increases the spread of emission and ion re-deposition.

3.1.3. Detailed magnetic shadowing of the density The background plasma density, therefore flux and erosion can be further shaped by magnetic shadowing. According to the simple SOL model [11] and as reflected in the background plasma profiles provided by EDGE2D-Eirene, the density decays exponentially from the last closed field surface (LCFS) to the wall at a rate given by the decay length (λ). The model further assumes a constant perpendicular diffusion coefficient, establishing the relationship between λ and the connection length (L_C) at each point. That is, λ varies spatially describing a faster decay (i.e., shadowing) of the density in areas with shorter L_C (see Section 3.1.2 and the detail mathematical description below, Eq. 3 and there on).

The earlier ERO study of JET OWL erosion already included a simplified model for shadowing, referred as 'crude shadowing model' in what follows. The model assumed that surface areas with $L_C \geq 42$ m were fully plasma wetted (i.e., no scaling of the decay length or density was applied). The surface was fully shadowed ($\lambda \sim 0$) elsewhere. A more detailed model, in which the density was scaled by zones according to averaged connection lengths for each area, was implemented in ERO by Ding *et al.* [27] for modeling of EAST proxy tiles. In the present exercise, magnetic shadowing is implemented in a similar way, but further refining the latter approach.

As mentioned above and described in Sections 2.2 and 3.1.1, the density profile provided by EDGE2D-Eirene is extrapolated to the ERO surface assuming an exponential decay: $n_e(r) = n_e(LCFS) \cdot \exp(-\Delta r/\lambda)$, where Δr is the radial distance measured from the LCFS to the surface, and λ is the density decay length, constant across the edge plasma. Here, to account for magnetic shadowing, λ is assumed to remain constant from the LCFS up to the radial location of the limiter tip: $\lambda(r = LCFS) = \lambda(r = r^{tip}) \equiv \lambda^{tip}$; but for surface cells (ij) located radially further towards the surface, λ varies according to the local connection length ($L_C(r^{ij}) \equiv {L_C}^{ij}$):

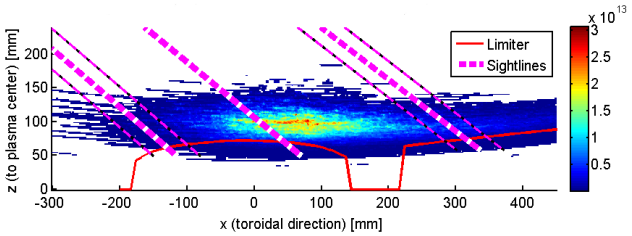

(a) small $D_\perp = 0.4$ mm^2/s

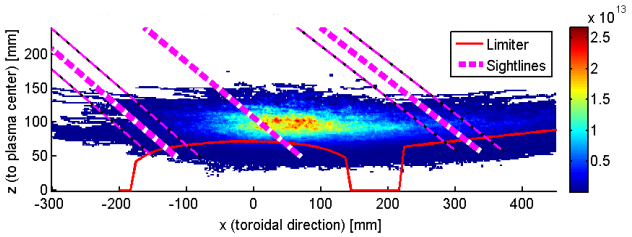

(b) simple SOL $D_\perp \sim 0.12$ m^2/s

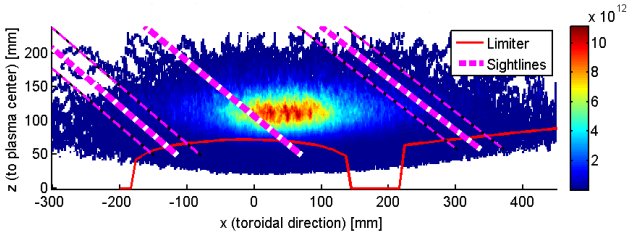

(c) Bohm $D_\perp \sim 20$ m^2/s

Figure 3: The 2D projection, integrated along the poloidal direction (y-axis), of Be II emission [ph/(sr·s·cm^2)] for the different perpendicular diffusion coefficient values tested in ERO: (a) $D_\perp = 0.4 \cdot 10^{-6}$ m^2/s; (b) assuming simple SOL model, $D_\perp \sim 0.12$ m^2/s and; (c) Bohm's diffusion coefficient, $D_\perp \sim 20$ m^2/s. The red solid line is the projection of the limiter and antenna D surfaces. The pink dotted lines represent − left to right − the projection of D12, D13 and D14 sightlines used in ERO. For color version of this figure, the reader is referred to the online version of this article.

$\lambda(r > r^{tip}) = \lambda(r = r^{ij}) \equiv \lambda^{ij})$. For a simple SOL model [11, 12] and a constant perpendicular diffusion coefficient ($D_\perp$), the variation of λ with L_C is given by:

$$D_\perp = \frac{\lambda^2 c_S}{L_C} = constant \implies \frac{{\lambda_{ij}}^2}{{\lambda_{tip}}^2} = \frac{{L_C}^{ij}}{{L_C}^{tip}} \implies \lambda_{ij} = \lambda_{tip}\sqrt{\frac{{L_C}^{ij}}{{L_C}^{tip}}}. \tag{3}$$

Thus, the shadowed density ($n_e{}'(ij)$) for a given cell (ij) is:

$$n_e{}'(ij) = {n_e}^{tip} \exp(-\Delta r'/\lambda_{ij}), \tag{4}$$

where ${n_e}^{tip}$ is the density at the radial distance of the limiter tip and $\Delta r' = r_{tip} - r_{ij}$.

Finally, the relative change due to shadowing can be expressed in terms of a local shadowing factor:

$$fne = \frac{{n_e}'(ij)}{n_e(ij)} = \exp[(\Delta r'/\lambda_{ij}) \cdot (1 - \sqrt{{L_C}^{ij}/{L_C}^{tip}})], \quad (5)$$

The L_C for each ERO surface cell (referred as 'local' in what follows) has been calculated by PFCFLUX [30]. As shown in the sequence of Fig. 4 and compared to using the 'crude shadowing model', the new density pattern shows an additional plasma wetted area on the limiter surface away from the neighboring antenna D. This additional flux increases the total Be erosion by a factor of 2. The new erosion area mainly contributes to emission in the vicinity of the D12 sightline, reducing asymmetries (i.e., D14/D12 ratios). Therefore, we conclude that the choice of shadowing model affects the outcome mainly qualitatively.

Given that background plasma flux reaching a given surface cell may cross neighboring regions with different connection lengths, 'shadowing by L_C zones' has also been implemented. In this model, similar to that used by Ding *et al.* [27], the surface is divided into zones, defined by all cells with a L_C within a given range and the mean L_C value is assigned to the entire zone (Table 1, 'mean'). The difference in erosion or emission between the local implementation of shadowing and that by zones is negligible.

Further, a second set of L_Cs has been assigned to the different zones (Table 1, 'low'): the mean L_C was lowered by about 2 orders of magnitude for all zones but the 1st one, setting a bigger difference between the main erosion area and elsewhere. This change in L_Cs allows to test the sensitivity of the model to the choice of L_Cs assigned to each zone, and to understand the absence of clear erosion zone patterns (observed in other ERO cases that applied shadowing [27, 31]).

Increasing the weight of the main erosion zone neither lead to a sharp erosion pattern. Following Eq. 5, we note that not only L_C, but also Δr defines the shadowing factor applied to density. In fact, Δr may have a larger effect than L_C, as the square root of the latter term is calculated. Therefore, in the present geometry and with a smoothly varying D flux pattern, a continuous transition from plasma wetted to shadowed areas is found.

Although developed during the present exercise, ERO studies being performed simultaneously have already incorporated this local shadowing model [31, 8]. Finally, note that the detailed shadowing model developed here is intended for localized erosion studies, such as in the present system, with well defined L_Cs and a prominent reference point or 'tip' : the area located radially closest to the LCFS and thus, with longest (yet finite) L_Cs. Therefore, this model may not apply for instance to limiter discharges, where $L_C \rightarrow \infty$ in areas in contact with core plasma; or to whole device modeling, where various 'tips' may be present.

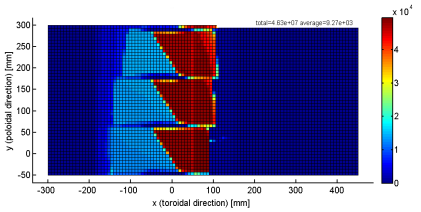

(a) Connection length, L_C

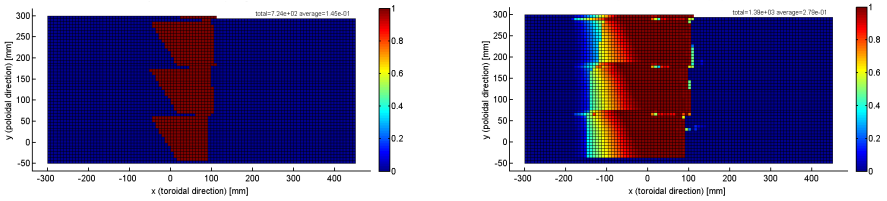

(b) Shadowing factor, fne

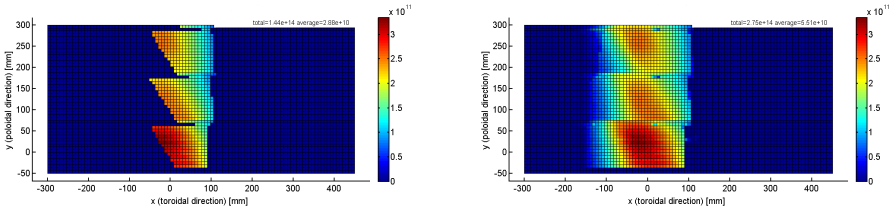

(c) Shadowed density, n'_e

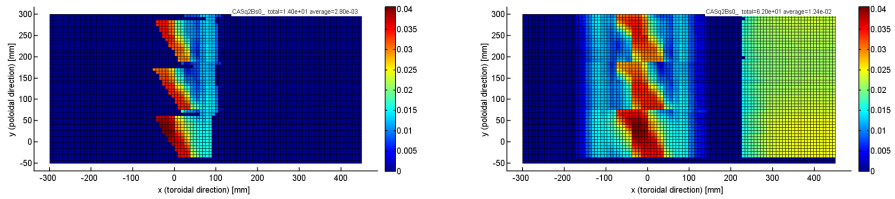

(d) Effective erosion yield

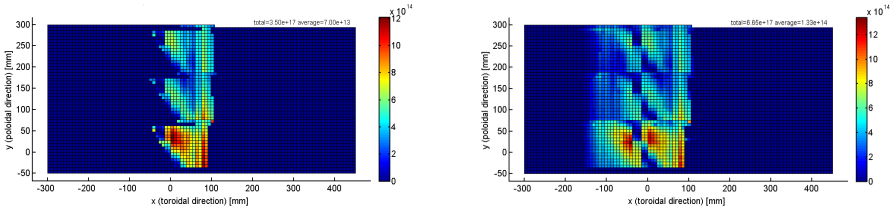

(e) Be erosion

Figure 4: (a) The connection length given by PFCFLUX for each ERO cell is used to calculate (b) the shadowing factor fne for each model: the 'crude shadowing' (left) and according to the more detailed approach, by connection length zones (right). These shadowing models results in the different patterns of (c) plasma density, (d) effective erosion yield and (e) Be erosion. For color version of this figure, the reader is referred to the online version of this article.

Table 1: Connection length ranges that define the zones used in the detailed magnetic shadowing model, and effective L_C values used in each zone, assuming: L_Cs to be the mean value of that given by PFCFlux for each area (${L_C}^{MEAN}$); or $\sim$ 2 orders of magnitude lower L_Cs (than ${L_C}^{MEAN}$) everywhere, except in Zone 1, used for sensitivity analysis(${L_C}^{LOW}$).

ZONE	L_C range [mm]	${L_C}^{MEAN}$ [mm]	${L_C}^{LOW}$ [mm]
1	$\geq 3.0 \cdot 10^4$	$4.6 \cdot 10^4$	$4.8 \cdot 10^4$
2	$1 - 3 \cdot 10^4$	$1.5 \cdot 10^4$	$5 \cdot 10^2$
3	$1 - 10 \cdot 10^3$	$8.0 \cdot 10^3$	$1 \cdot 10^1$
4	$0.1 - 10 \cdot 10^2$	$3.0 \cdot 10^2$	1.0
5	≤ 10	0.0	0.0

3.1.4. Including CX neutral fluxes The study of erosion due to plasma surface interactions often focuses on degradation of plasma-wetted components and parameters affecting it (e.g., Refs. [7, 9] and Sections 3.1.1, 3.1.3 and 3.1.5 in this paper). However, plasma-shadowed surfaces can also contribute to impurity production. Neutrals, which are not confined by the magnetic field and therefore equally impact exposed and recessed surfaces, can gain energy through charge exchange (CX) processes taking place in the scrape-off layer. Fluxes of these energetic CX neutrals dominate erosion of recessed components, such as antennas, and have therefore been included in the present model.

The EDGE2D-Eirene simulations that provided background plasma parameters also output CX neutral fluxes (for D_0, Be and D_2). These 1D flux profiles are obtained for each segment (L) that runs between (R_1,Z_1) and (R_2,Z_2), drawing draw a cross-section of JETs wall: $L = \sqrt{(R_1 - R_2)^2 + (Z_1 - Z_2)^2}$. Toroidal symmetry is assumed to transform these 1-D profiles into 2D-fluxes (Γ) for ERO: $\Gamma = C/(A \cdot e)$, where C is the 1-D profile outputted by EDGE2D-Eirene (as a 'current'), e is the elementary charge and A the area covered by L: $A = 2\pi L \cdot (R_1 + R_2)/2$.

The sputtering yield for CX neutrals, $Y_{CX}(E_{CX}, \alpha_{CX})$ is calculated using the Eckstein 2007 fit formula [19, 20]. A Maxwellian distribution is assumed for the impact energy, E_{CX}:

$$f(E_{CX}) = 2\sqrt{E_{CX}/\pi} \cdot (k_B T_n)^{-3/2} \exp(-E_{CX}/k_B T_n), \tag{6}$$

where T_n is the neutrals' temperature. The radial profile of T_n is provided by EDGE2D-Eirene. However, the radial location where neutrals gain energy through CX processes is not well known. Thus, different assumptions have been tested for T_n and the related impact angle, α_{CX}:

i T_n at the EDGE2D-Eirene grid border (towards the wall), representing T_n at the limiter surface in ERO, where erosion is evaluated. The region between the outermost grid surface of EDGE2D and the physical wall is assumed a vacuum

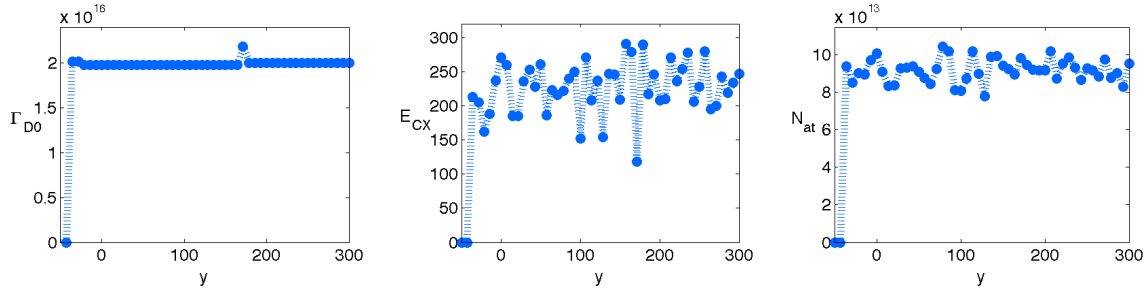

(a) CX D_0 flux (b) CX D_0 impact energy (c) Number of atoms eroded

Figure 5: Poloidal profiles of (a) CX neutral fluxes for D_0, Γ_{D_0}, calculated by EDGE2D-Eirene; (b) their impact energies, E_{CX}, calculated assuming a Maxwellian distribution for neutrals' temperature T_n at $\rho = 0.95$; and (c) number of particles eroded, N_{D_0}, for Γ_{D_0} and E_{CX} shown in this figure; obtained around the toroidal location $x = 0$

region, so no significant radial gradients in T_n are expected. CX neutrals are assumed to be generated with a random uniform distribution of angles. As these fluxes are not affected by electromagnetic forces and thus keep their initial distribution in velocity, neutrals will reach the wall with a $cos(\alpha_{CX})$-like distribution of angles, with α_{CX} between $(0, \pi/2)$.

ii T_n at $\rho \sim 0.95$, closer to where most CX processes take place. As the mean free path of neutrals is $\sim 10 - 15$ cm [32], of the order of the distance from $\rho \sim 0.95$ to the wall, only neutrals traveling nearly in the radial direction will reach the surface, impacting at approximately normal incidence ($\alpha_{CX} = 0$).

Finally, the contribution of CX neutrals to the total erosion of a cell − in number of eroded particles − can be calculated as:

$$N_{CX} = \sum_{D_0, Be, D_2} \Gamma \cdot Y_{CX} \cdot A_{cell}, \tag{7}$$

where A_{cell} is the cell area. For illustration, the poloidal profiles at the midplane of D_0 flux, impact energy ${E_{CX}}^{D0}$ and consequent Be erosion are shown in Figure 5.

The impact of CX neutral fluxes on erosion and emission has been evaluated by source, i.e., by the relative contribution of CX neutrals to the total erosion (N_{CX}/N_{TOT}) − the other source being the background plasma. As shown in Table 2, CX neutrals contribute to the total erosion and emission by 15-50% (assuming the source temperature T_n at the wall or at $\rho = 0.95$, respectively).

The impact of including CX neutrals has also been evaluated by component, where the contribution of CX neutrals is analyzed separately for the limiter and antenna (Table 3). The same erosion model is applied to both components, thus the contribution of each region to the total CX neutral erosion will be proportional to the exposed area:

$$N_{CX}^{lim} = N_{CX} \cdot (A_{lim})/(A_{lim} + A_{ant}), \tag{8}$$

Table 2: Comparison between Be erosion and emission (integrated over the entire simulated surface and volume, respectively) generated by each source, expressed as the contribution of CX neutrals, the total (sum of CX neutrals and background plasma) and ratio of the two. Erosion is given in units of [10^{16} atoms] and emission in [10^{16} Photons/volume].

Observable	CX model, T_n	by CX	Total	Fraction by CX
Eros.	wall	8.47	43.5	0.20
Eros.	$\rho = 0.95$	35.1	70.1	0.50
Be I	wall	0.47	2.55	0.18
Be I	$\rho = 0.95$	1.97	4.05	0.49
Be II	wall	0.46	2.74	0.17
Be II	$\rho = 0.95$	1.96	4.24	0.46

Table 3: Comparison of the contribution of the different sources (CX neutrals and background plasma) to the total erosion of each component. The contribution of CX neutrals (e.g., to the limiter) is proportional to exposed area: $N_{CX}^{lim} = N_{CX} \cdot (A_{lim})/(A_{lim} + A_{ant})$ (see the main text for notation and details). Note that antenna D is only exposed to erosion by CX neutrals. Erosion is integrated across the entire surface and given in units of [10^{16} atoms].

Component	CX model, T_n	by CX	Total	Fraction by CX
Limiter	wall	4.92	39.9	0.12
Limiter	$\rho = 0.95$	20.3	55.3	0.37
Antenna D	wall	3.58	3.58	1.0
Antenna D	$\rho = 0.95$	14.8	14.8	1.0

where N_{CX}^{lim} and N_{CX} are the limiter total erosion by CX neutrals, respectively. A_{lim} and A_{ant} are the limiter and antenna D surface areas exposed to CX neutrals, 58% and 42% of the total area exposed to neutrals, respectively. Due to magnetic shadowing (for any of the models discussed in Section 3.1.3), only the limiter is exposed to erosion by the background plasma, while CX neutrals cause 100% of the antenna D erosion. In contrast, CX neutrals contribute by $(15 - 35\%)$ to the total erosion of the limiter. Note that the contribution of CX neutrals to emission is not analyzed by component, as volumetric observables (e.g. emission) are harder to evaluate than those by area (e.g. erosion) and the similar 'fraction by CX' is found for the three observables in the analysis by source (Table 2).

3.1.5. Erosion yields accounting for angular and energy distribution of the background plasma under biasing Plasma particles in the scrape-off layer are likely to impact on

a surrounding surface. The magnetic field geometry and sheath structure are known to modify these impact distributions, and the angle and energy of the impacts greatly affects the probability for consequent sputtering (see Refs. [22, 33, 34] and references therein).

In the first ERO study of enhanced Be erosion [10], normal incidence for the background plasma ions was assumed, and biasing (V_{bias}), which represents the sheath perturbation, was only introduced through modifying the impact energy (E_{in}) [35]:

$$E_{in} = 2 \cdot T_i + Z_{imp} \cdot \left[V_{bias} - T_e \cdot \log \left(\frac{2 \cdot \exp(e k_B T_e)}{1 + \exp(-V_{bias}/T_e)} \right) \right], \tag{9}$$

where T_i and T_e are the plasma ion and electron temperatures, respectively; Z_{imp} is the average charge state of the impurity, k_B is the boltzmann constant and e is the elementary charge.

However, sheath perturbations can modify both impact energy and angular distributions. In order to account for such effects, trajectories of D and Be ions (that represent the background plasma) across the sheath are calculated analytically, varying the biasing voltage and accounting for the present oblique magnetic configuration. These distributions, together with the Eckstein fitting formula for sputtering cited above, are used to calculate effective yields of erosion by the background plasma, as a function of the local plasma temperature and magnetic field angle [22].

As the yields used in the reference case assume a fixed $V_{bias} = 0$ (see Section 2.3), and to highlight the synergetic effects between biasing and impact distributions under an oblique magnetic field, the outcome of this section is compared to the earlier OWL ERO model (instead of the reference case). Incorporating the new yields lead to quantitative changes in the output, with a 4 fold uniform increase in Be erosion and emission. The increase by a factor of 2-3 with biasing is also reproduced. Only a slight variation in surface patterns is observed, shifting the erosion peak (around the limiter tip) away from the antenna D.

3.1.6. Including erosion of beryllium as deuteride molecules Despite being a metal, a fraction of the eroded Be can be released as molecules under continuous deuterium plasma exposure, most commonly in the form of beryllium deuteride (BeD) [36]. This molecular erosion is caused by swift chemical sputtering (SCS) (also known as chemically assisted physical sputtering, CAPS), a non-thermal process, with a defined impact energy threshold, known to participate in the erosion of carbides [37] and later understood to also affect a wider range of materials [38]. These deuteride molecules can penetrate deeper into the plasma than atomic impurities before dissociating and being ionized, thus altering emission patterns.

In the present study, two different approaches to estimating the BeD source have been evaluated. Molecular contributions can be taken as a fraction of the yields already calculated for the background plasma (Section 3.1.5). Such case assumes that Be − an

impurity present in the edge plasma − also contributes to production of BeD molecules. In fact, this process has been observed in Molecular Dynamics (MD) simulations [39], although its contribution to BeD production is not well quantified yet. The second approach assumes that the molecular yield is a fraction of the yield obtained for a pure D background plasma.

Similar erosion and emission is observed with either molecular erosion model. Overall, the largest impact is found in the Be II emission pattern (Fig. 6(b)), as BeD dissociates and ionizes further from the source than atomic Be, leading to spreading of Be II emission away from the surface (Fig. 6(b)). However, no significant changes ($\leq 10\%$) are found in erosion or emission − either locally measured by the sightlines or integrated over the entire simulation volume.

Finally, note that despite the effort to fully characterize molecular emission, large uncertainties remain due to the inter-dependence of parameters affecting erosion (e.g., substrate temperature, D concentration and plasma flux) [40]. A recent multi-scale study [23] has tested a promising workflow to reduce uncertainties in erosion yields: Object Kinetic Monte Carlo simulations, parameterized from first principle calculations and run under experimental-like conditions are used to obtain the equilibrium D and vacancy profiles at different substrate temperatures. Then, MD substrates (of crystalline Be) are modified to incorporate these D and vacancy distributions, and irradiated with D at various impact energies (and keeping the different substrate temperatures) to calculate erosion yields and molecular fractions. Therefore, this approach also overcomes the long-standing issue of unrealistically high fluxes used in MD studies of irradiation effects in materials. However, the latest data − yields and BeD/Be ratios − were not available when the present ERO simulations were performed. Thus, BeD/Be erosion ratios calculated by earlier MD studies [41], which do not account for temperture or D concentration dependence and are of the order of $0.25 - 0.3$ are used in the present case.

3.2. Exploring the extended model and comparison to experiments

3.2.1. The extended model Finally, simulations that include new and improved models introduced in ERO, and best estimates of uncertain input parameters − based on the sensitivity analysis above − have been performed. Such cases were run with: the LCFS shifted 1 cm away from the wall; the perpendicular diffusion coefficient calculated for a simple SOL model; the density scaled according to the 'shadowing by zones' model; including erosion by CX neutrals assuming $E_{in}(T_n = T_{\rho=0.95})$; erosion by the background plasma calculated for sputtering yields that include analytically derived impact energy and angular distributions, under the present oblique magnetic field configuration and including biasing; and a fraction of Be being eroded in molecular form (as BeD).

Beryllium erosion and emission obtained for the complete model (Fig. 7) have been compared to the earlier ERO study [10], as well as to experiments (Table 4). Including additional erosion sources (CX neutrals and magnetic shadowing by zones) and erosion

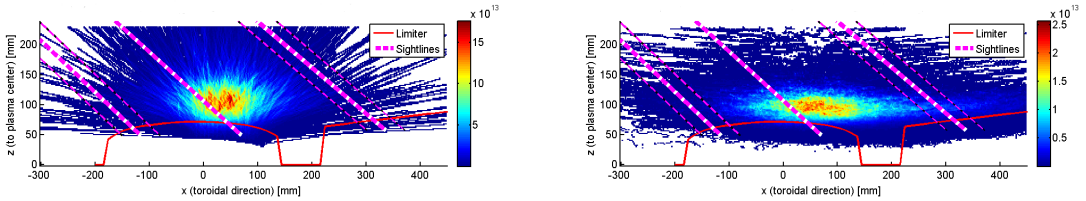

(a) BeD emission

(b) Be II emission

Figure 6: The 2D projection, integrated along the poloidal direction (y-axis), of (a) BeD (498 nm) and (b) Be II emission in units of [ph/(sr·s·cm^2)] calculated in ERO for the cases that include molecular erosion of Be. The BeD yield is taken as a fraction of the erosion caused by the background plasma. The red solid line is the projection of the limiter and antenna D surfaces. The pink dotted lines represent − left to right − the projection of D12, D13 and D14 sightlines used in ERO. For color version of this figure, the reader is referred to the online version of this article.

yields that account for the angular distribution of the background plasma, despite the 1 cm shift in LCFS away from the wall, increases Be erosion and emission by an order of magnitude, leading to observables (Be I and Be II emission) in the range of experimental values. However, the new erosion pattern (Fig. 7(a)) shifts Be emission away from the neighboring antenna D, missing the asymmetry observed experimentally and reproduced in the 1st ERO exercise. These changes also reveal that the emission asymmetry is strongly influenced by the density shadowing model, more e.g., than by erosion due to CX fluxes.

The same trend as in the 1st ERO model and experiments, with respect to biasing (V_{bias}, which represents toggling of the magnetically connected antenna C) is observed: erosion increases by a 2-3 fold with V_{bias} up to 100 eV and then saturates. However, in ERO, only erosion of plasma-wetted surfaces is affected by perturbations in the sheath (i.e., biasing). Therefore, emission − especially by neutral Be, Be I − can only increase with V_{bias} if the erosion source (i.e., plasma-wetted area) is located below the measured volume. Thus, under the current geometry, where surface areas below the analyzed sightlines (D12 and D14) are shadowed and the main erosion source is located around D13, enhanced erosion is not fully reflected as increased emission. Emission of Be II partly reflects the increase in erosion with biasing, as ionized Be and thus Be II light is carried towards the D14 sightline by the current flow velocity pattern. Further, note that increasing RF-power ($V_{bias} \sim 100$ eV) does indeed increase emission of Be I and Be II light (by $\sim$ 2-fold) observed by the D13 sightline in ERO.

To better reproduce the experimental outcome −maintaining the additional erosion sources, but recovering the asymmetry achieved in the earlier exercise [10]− ERO simulations including all new implementations but using the 'crude shadowing model' have been performed. As shown in Figs. 8(b) and 8(c), the outcome − Be I and Be II

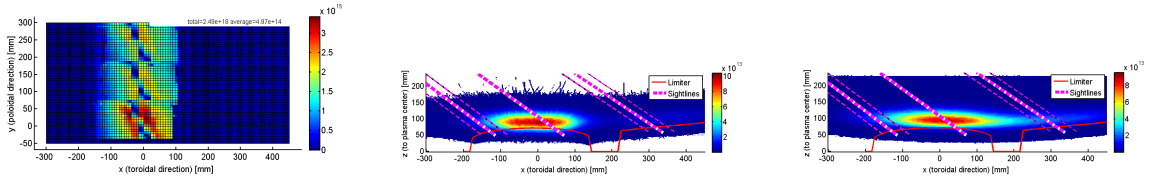

(a) Be erosion (b) Be I emission (c) Be II emission

Figure 7: Output of ERO simulations run including new and improved models introduced in ERO and best estimates in uncertain input parameters: (a) Be erosion of each surface cell, including that by the background plasma and CX neutrals, for $V_{bias} = 100$ eV; (c) − (d) The 2D projection, integrated along the poloidal direction (y-axis), of Be I and (d) Be II emission, respectively, in units of [ph/(sr·s·cm^2)] for $V_{bias} = 100$ eV. The red solid line is the projection of the limiter and antenna D surfaces. The pink dotted lines represent − left to right − the projection of D12, D13 and D14 sightlines used in ERO. For color version of this figure, the reader is referred to the online version of this article.

Table 4: comparison between Be I (top) and Be II (bottom) emission [10^{12} ph/(sr·s·cm^2)] observed experimentally ('exp') and calculated by ERO using all features of the extended model, when the remote antenna C is OFF ($V_{bias} = 0$ eV) and ON ($V_{bias} = 100$ eV). Intervals given for the experimental values correspond to observations performed with different magnetic pitch angle ($q-95$) sweeping [1]. Intervals given for ERO correspond to emission values measured assuming sightlines of different sizes ($R = 20 - 50mm$).

signal	sightline	OFF ERO	exp.	ON ERO	exp
Be I	D12	$1.6 - 2.0$	$0.4 - 0.6$	$2.6 - 3.4$	1.8
	D14	1.0	$1.0 - 2.0$	$1.0 - 1.1$	$5. - 8.$
Be II	D12	$1.7 - 1.9$	$0.8 - 1.2$	$2.9 - 3.4$	$2. - 3.$
	D14	$2.0 - 2.1$	$1.5 - 2.2$	$3.0 - 3.1$	$5. - 6.5$

emission, measured by D12 and D14 sighlines − is in good agreement with experiments when the remote antenna C is off ($V_{bias} = 0$). However, as discussed above, while the increase in the simulated erosion with biasing (Fig. 8(a)) is about the same as the increase in the emission measured by the sightlines ($2 - 3$ fold), the latter is not fully reflected in the simulated emission, especially for Be I.

The Be I emission underestimated (in the new simulations), especially when the distant antenna C is ON ($V_{bias} > 0$) and for the emission region near the D14 sightline, cannot be compensated by amplifying the effect of any of the sources discussed so far: neutrals are assumed to be unaffected by the sheath and thus, biasing potential; changes in plasma profiles due to shifts in the LCFS position affect equally all sightlines and

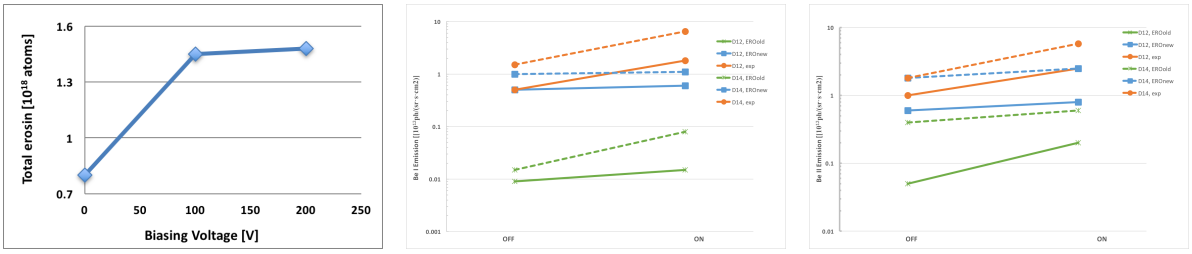

(a) Be erosion (b) Be I emission (c) Be II emission

Figure 8: Output of ERO simulations run using the 'best match' parameters set, i.e., including all new and improved models, and best estimates in uncertain input parameters, but using the 'crude shadowing model': (a) integrated Be erosion as a function of biasing voltage, in units of [10^{18} atoms)]; (b) − (c) Be I and Be II emission (respectively) observed by the D12 (solid lines) and D14 (dashed lines) sightlines, in the earlier ERO exercise (ERO-old, green), the present study (ERO-new, blue) and experiments (orange), in units of [10^{12} ph/(sr·s·cm^2)]. For color version of this figure, the reader is referred to the online version of this article.

under all biasing potentials; and different sputtering yield and magnetic shadowing models leave unaffected shadowed areas such as near the spot of the D14 sightline. Therefore, differences between the ERO model and experimental outcome may hint at further local erosion sources that are not captured in the present study, likely near interception area of the D14 sightline and neighboring antenna surface.

Present understanding is that the remote interaction is not with the remote antenna C per-se, but with the remote antennas own lateral protection limiters, where near-fields also appear (see e.g. Fig. 1 in Ref. [10]). Furthermore, currently emerging models of RF sheath propagation in the SOL [42] provide mechanisms for transport of locally rectified sheath potentials to remote PFCs even overcoming conductive protrusions, such as poloidal limiters which would otherwise block direct magnetic connection between observed limiter and remote, active antenna. In the experiment being modeled here, the limiter to the right of antenna D acts as such intermediate protrusion. Although not directly observed in the experiment, it is reasonable to assume that there was RF-PSI at that interception as well and that any Be ions from that interaction could contribute to the observed emission (i.e. adding to the Be II signal) by transport along the same field lines to the observed limiter.

Furthermore, we highlight that CX neutral fluxes and their impact energy are assumed to be independent of antenna toggling. However, RF-power can modify local plasma conditions, and thus, production of energetic neutrals. This effect could increase the contribution of erosion by CX neutral fluxes to emission, especially near the neighboring antenna D, when the remote antenna C is ON.

3.2.2. Reducing uncertainties in the input Throughout this article we have identified parameters and models that introduce uncertainties in erosion and impurity transport modeling. Some of the limitations, as attempted in the present exercise, can be overcome implementing more complete models (e.g., Section 3.1.3) and looking into secondary sources (e.g., Sections 3.1.4 and 3.1.6). However, uncertainties could further be restrained through inter-disciplinary work.

For instance, the input in background plasma parameters, which largely determine fluxes to the wall and thus erosion, can be improved. Often, such as in the present case, fluid models use plasma measurements (e.g., n_e and T_e) in one location to calculate conditions elsewhere. Although widely used, this approach can be insufficient, due to lack of an adequate radial ion transport model (see Refs. [16, 43] and references therein). Measurements in or near the location of interest (or at a toroidally symmetric point) can greatly improve the input to erosion and impurity transport modeling for reproducing the experimental outcome [27]. Also, using 3-D fluid codes, which can better capture the complex wall geometry, and extending their grid to the wall, thus not needing to extrapolate plasma parameters assuming a given decay model, may reduce uncertainties. Further, measurements of neutral fluxes for different species and temperatures when reaching the wall (i.e., impact energies) can greatly help to estimate erosion of recessed components, which is necessary not only for validation of local erosion modeling, but also for a better balance of global erosion and re-deposition.

More accurate description of the walls' response to plasma, studied by further characterization of plasma-exposed surface and modeling of irradiation effects in plasma facing materials, can also result in better input for erosion and impurity transport modeling. For example, as described in Section 3.1.6 [23], multi-scale modeling allows for characterization of materials' response at the atomic scale (sputtering) under realistic surface conditions (implantation profiles obtained for experimetal fluxes, at different substrate temperatures). Our model could be further improved by including chemical and mixed-material effects in the sputtering databases [44].

Moreover, mathematical methods, such as uncertainty quantification techniques [45, 46] can be applied to identify input parameters with greatest impact on output, instead time-consuming scans, post-processing and evaluation run by hand, for various (but an incomplete set of) input parameters.

Finally, we highlight that predictive modeling can be used to optimize or select key diagnostics, which in return improve the input data and allow better benchmarking of the code. Such approach has been applied by Klepper *et al.* [47] in experiments similar to the cases discussed here [1]. Based on earlier [10] and present ERO simulations, the D13 sightline, where most of erosion by the background plasma takes place, and BeD emission channel, which reveals BeD production for benchmarking of the multi-scale model, were added to the set of diagnostics used.

4. Conclusions

Experiments at JET showed enhanced, asymmetric Be erosion due to sheath perturbations introduced by magnetically connected ICRH antennas. A first modeling effort performed using the 3D impurity transport code ERO reproduced qualitatively the experimental outcome. In the present study, we have revisited the ERO model, improving simplified descriptions to be consistent with the models providing input (e.g., background plasma and surface description) and implementing further processes impacting erosion. Sensitivity analysis of these new implementations and further ERO input parameters with largest uncertainties have allowed for better understanding of the impact of each process in the output, a more reliable quantitative comparison to experiments and identification of fields in which further work would reduce most uncertainties in erosion and impurity transport modeling.

In greater detail, the present article addressed: i) The magnetic configuration, which adjusted to the present case (compared to that used to for calculating the background plasma) suggests a shift in the LCFS position by 1 cm inward, leading to lowering of erosion by a factor 5; ii) The perpendicular diffusion coefficient, a parameter hard to measure or calculate from first principles. Varying its value within a wide (8-orders of magnitude) range of values, from negligible to that estimated as maximum for the local plasma conditions, showed that higher diffusion values lead to small, yet non-zero re-deposition, but had a negligible impact in Be emission; iii) The model for shadowing of the density, which has been modified to account for spatially varying connection lengths. The local implementation of shadowing introduced qualitative changes in ERO, generating an additional surface erosion area in the limiter and shifting Be emission away from the neighboring antenna; iv) Erosion caused by neutrals energized through charge-exchange processes, which is estimated to be the main sputtering source for recessed components, such as antennas. Introducing these new fluxes increased the overall erosion by $15 - 50\%$. As neutrals affect equally all surfaces and the neighboring antenna D is shadowed from the plasma, this erosion source shifts Be emission away from the limiter; v) Impact energy and angular distributions for the ions in the background plasma. Introducing new erosion yields, which include such distributions derived analytically, increased erosion by a factor of 4; vi) Chemical effects in sputtering of Be that cause erosion in molecular form (as BeD). Including release of BeD has a negligible impact in emission as measured by the sightlines, although Be II light reaches further from the surface due to the larger penetration of BeD molecules (compared to atomic Be).

Running ERO with input based on sensitivity analysis' outcome, and including improved and new models, results in emission (measured by D12 and D14 sightlines) within the experimental range and an order of magnitude higher than that reported by the 1st ERO study. The trend with respect to biasing is maintained, with a 2-3 fold increase in erosion and emission up to $V_{bias} \sim 100$ eV, then saturating. However, this effect is not fully captured by emission observed by the sightlines in ERO, as erosion

by background plasma (the only source affected by the enhanced sheath) mainly takes place in between D12 and D14. Further, the D14-to-D12 asymmetry − experimentally found and reproduced by the earlier ERO model − is no longer observed when the detailed shadowing model is used. This shift in emission further highlights that the implementation of a local shadowing model dominates over the effect of CX neutral fluxes. Therefore, ERO simulations with the same set of parameters, but assuming the crude shadowing model have also been performed. The outcome reproduces the experimental Be I and Be II signals for both D12 and D14 sightlines when the magnetically connected antenna is off ($V_{bias} = 0$ eV). However, as mentioned above, Be light emitted by the main erosion source and enhanced by biasing is not fully captured by either D12 or D14 and emission is underestimated in ERO when the remote antenna is on ($V_{bias} \sim 100 - 200$ eV).

Further, we highlight that uncertainties can be further reduced through inter-disciplinary collaboration, such as using uncertainty quantification techniques to identify the most influential input parameters. Uncertainties in surface erosion data can also be reduced by using multi-scale modeling workflows, such as the MD-KMC simulations recently performed to calculate Be sputtering and molecular erosion yields, including surface temperature and composition dependence. Furthermore, better local diagnostics could significantly improve the confidence in the plasma parameters used, as modeling cannot always recreate conditions in the location of interest. Also, diagnostics of neutral fluxes and energies would allow for better estimates and model validation of erosion of recessed components. These measurements may also help understanding the dependence of CX neutral fluxes on RF-induced variation of local plasma conditions. Finally, we highlight that predictive modeling can identify key diagnostics for experiments that in return improve with model validation. For example, the BeD emission channel and D13 sightline have been recognized as diagnostics necessary to fully characterize the present case, and therefore, were included in the latest JET experiments of enhanced Be erosion due to magnetically connected antennas.

Acknowledgments

This material is based upon work supported by the U. S. Department of Energy, Office of Science, Office of Fusion Energy Sciences and Office of Advanced Scientific Computing Research through the Scientific Discovery through Advanced Computing (SciDAC) project on Plasma-Surface Interactions. Authors of this manuscript are affiliated with Oak Ridge National Laboratory (ORNL), which is managed by UT-Battelle, LLC for the U.S. Department of Energy under Contract No. DE-AC05-00OR22725.
This work has been carried out within the framework of the EUROfusion Consortium and has received funding from the Euratom research and training programme 2014-2018 under grant agreement number 633053 and from Tekes the Finnish Funding Agency for Innovation under the FinnFusion Consortium. The views and opinions expressed herein

do not necessarily reflect those of the European Commission.

References

[1] C.C. Klepper and P. Jacquet and V. Bobkov and L. Colas and T.M. Biewer and D. Borodin and A. Czarnecka and C. Giroud and E. Lerche and V. Martin and M.-L. Mayoral and F. Rimini and G. Sergienko and D. Van Eester. RF sheath-enhanced beryllium sources at JETs ICRH antennas . *Journal of Nuclear Materials*, 438, Supplement:S594 – S598, 2013. Proceedings of the 20th International Conference on Plasma-Surface Interactions in Controlled Fusion Devices.

[2] L. Colas and J.P. Gunn and I. Nanobashvili and V. Petrlka and M. Goniche and A. Ekedahl and S. Heuraux and E. Joffrin and F. Saint-Laurent and C. Balorin and C. Lowry and V. Basiuk. 2-D mapping of ICRF-induced SOL perturbations in Tore Supra tokamak . *Journal of Nuclear Materials* , 363365:555 – 559, 2007. Plasma-Surface Interactions-17.

[3] C. E. Thomas, Jr. and J. H. Harris and G. R. Haste and C. C. Klepper and J. T. Hogan and S. Tobin and F. W. Baity and R. C. Isler and T. Uckan and D. B. Batchelor and M. D. Carter and P. M. Ryan and D. J. Hoffman and B. Saoutic and B. Beaumont and A. Becoulet and H. Kuus and D. Fraboulet and A. Grosman and D. Guilhem and W. Hess and J. Walter and T. Loarer and M. Chatelier and the Oak Ridge National Laboratory/Fusion Energy Division Team and Equipe Tore Supra. ICRF/Edge Interaction Guidelines for ICRF Antenna Design and Initial ICRF/Edge Interaction Experiments on the Tore Supra Tokamak. *Fusion Science and Technology*, 30:1–39, 1996.

[4] Bobkov, Vl V. and Braun, F. and Dux, R. and Herrmann, A. and Giannone, L. and Kallenbach, A. and Krivska, A. and Mueller, H. W. and Neu, R. and Noterdaeme, J. -M. and Puetterich, T. and Rohde, V. and Schweinzer, J. and Sips, A. and Zammuto, I. and ASDEX Upgrade Team. Assessment of compatibility of ICRF antenna operation with full W wall in ASDEX Upgrade. *Nuclear Fusion*, 50:035004, 2010.

[5] Wukitch, S. J. and Lipschultz, B. and Marmar, E. and Lin, Y. and Parisot, A. and Reinke, M. and Rice, J. and Terry, J. and C-Mod Team. RF plasma edge interactions and their impact on ICRF antenna performance in Alcator C-Mod. *Journal of Nuclear Materials*, 363-365:491–497, 2007.

[6] Bobkov, Vl. and Arnoux, G. and Brezinsek, S. and Coenen, J. W. and Colas, L. and Clever, M. and Czarnecka, A. and Braun, F. and Dux, R. and Huber, A. and Jacquet, P. and Klepper, C. and Lerche, E. and Maggi, C. and Marcotte, F. and Maslov, M. and Matthews, G. and Mayoral, M. L. and McCormick, K. and Meigs, A. and Milanesio, D. and Monakhov, I. and Neu, R. and Noterdaeme, J. -M. and Puetterich, Th. and Rimini, F. and Van Rooj, G. and Sergienko, G. and Van Eester, D. and JET EFDA Contributors. ICRF specific plasma wall interactions in JET with the ITER-like wall. *Journal of Nuclear Materials*, 438:S160–S165, 2013.

[7] D Borodin, S Brezinsek, J Miettunen, M Stamp, A Kirschner, C Bjrkas, M Groth, S Marsen, C Silva, S W Lisgo, D Matveev, M Airila, V Philipps, and The JET-EFDA Contributors. Determination of be sputtering yields from spectroscopic observations at the jet iter-like wall based on three-dimensional ero modelling. *Physica Scripta*, 2014(T159):014057, 2014.

[8] D. Borodin, S. Brezinsek, I. Borodkina, M. Probst, C. Björkas, A. Kirschner, J. Romazanov, J. Miettunen, M. Groth, Ch. Linsmeier, and JET Contributors. Modelling of be erosion in jet and extrapolation of the data for iter, 2016. 26th IAEA proceedings.

[9] S. Brezinsek, M.F. Stamp, D. Nishijima, D. Borodin, S. Devaux, K. Krieger, S. Marsen, M. O'Mullane, C. Bjoerkas, A. Kirschner, and JET EFDA contributors. Study of physical and chemical assisted physical sputtering of beryllium in the jet iter-like wall. *Nuclear Fusion*, 54(10):103001, 2014.

[10] C C Klepper, D Borodin, M Groth, A Lasa, M Airila, V Bobkov, L Colas, P Jacquet, A Kirschner, A Terra, T M Biewer, E Delabie, C Giroud, and JET Contributors. Estimates of rf-induced erosion at antenna-connected beryllium plasma-facing components in jet. *Physica Scripta*, 2016(T167):014035, 2016.

[11] Peter C Stangeby. The Simple SOL and Ionization in the Main Plasma. In Peter Stott and Hans Wilhelmsson, editor, *The Plasma Boundary of Magnetic Fusion Devices*, pages 22–26. IoP, The Institute of Physics, London, 2007.

[12] K Uehara, Y Gomay, T Yamamoto, N Suzuki, M Maeno, T Hirayama, M Shimada, S Konoshima, and N Fujisawa. Gross particle confinement characteristics by the boundary plasma in the jft-2 tokamak. *Plasma Physics*, 21(1):89, 1979.

[13] A. Kaye and T. Brown and V. Bhatnagar and P. Crawley and J. Jacquinot and R. Lobel and J. Plancoulaine and P.-H. Rebut and T. Wade and C. Walker. Present and future JET ICRF antennae. *Fusion Engineering and Design*, 24(1):1 – 21, 1994.

[14] A. Kirschner, V. Philipps, J. Winter, and U. Kögler. Simulation of the plasma-wall interaction in a tokamak with the monte carlo code ero-textor. *Nuclear Fusion*, 40(5):989, 2000.

[15] D Borodin, A Kirschner, S Carpentier-Chouchana, R A Pitts, S Lisgo, C Björkas, P C Stangeby, J D Elder, A Galonska, D Matveev, V Philipps, and U Samm. Ero code benchmarking of iter first wall beryllium erosion/re-deposition against lim predictions. *Physica Scripta*, 2011(T145):014008, 2011.

[16] M. Groth, S. Brezinsek, P. Belo, M.N.A. Beurskens, M. Brix, M. Clever, J.W. Coenen, C. Corrigan, T. Eich, J. Flanagan, C. Guillemaut, C. Giroud, D. Harting, A. Huber, S. Jachmich, U. Kruezi, K.D. Lawson, M. Lehnen, C. Lowry, C.F. Maggi, S. Marsen, A.G. Meigs, R.A. Pitts, G. Sergienko, B. Sieglin, C. Silva, A. Sirinelli, M.F. Stamp, G.J. van Rooij, S. Wiesen, and the JET-EFDA Contributors. Impact of carbon and tungsten as divertor materials on the scrape-off layer conditions in jet. *Nuclear Fusion*, 53(9):093016, 2013.

[17] M. Groth and S. Brezinsek and P. Belo and G. Corrigan and D. Harting and S. Wiesen and M.N.A. Beurskens and M. Brix and M. Clever and J.W. Coenen and T. Eich and J. Flanagan and C. Giroud and A. Huber and S. Jachmich and U. Kruezi and M. Lehnen and C. Lowry and C.F. Maggi and S. Marsen and A.G. Meigs and G. Sergienko and B. Sieglin and C. Silva and A. Sirinelli and M.F. Stamp and G.J. van Rooij. Target particle and heat loads in low-triangularity L-mode plasmas in JET with carbon and beryllium/tungsten walls . *Journal of Nuclear Materials*, 438, Supplement:S175 – S179, 2013.

[18] M.I. Airila and A. Järvinen and M. Groth and P. Belo and S. Wiesen and S. Brezinsek and K. Lawson and D. Borodin and A. Kirschner and J.P. Coad and K. Heinola and J. Likonen and M. Rubel and A. Widdowson. Preliminary Monte Carlo simulation of beryllium migration during JET ITER-like wall divertor operation . *Journal of Nuclear Materials* , 463:800 – 804, 2015. Proceedings of the 21st International Conference on Plasma-Surface Interactions in Controlled Fusion Devices.

[19] W. Eckstein. Sputtering Yields. In R. Behrisch and W. Eckstein, editor, *Sputtering by Particle bombardment*, pages 32–189. Springer, Berlin, 2007.

[20] W. Eckstein. Corrections to Chapter 'The sputtering yield' in the book 'Sputtering'.

[21] L.L. Lao, H. St. John, R.D. Stambaugh, A.G. Kellman, and W. Pfeiffer. Reconstruction of current profile parameters and plasma shapes in tokamaks. *Nuclear Fusion*, 25(11):1611, 1985.

[22] I. Borodkina, D. Borodin, S. Brezinsek, A. Kirschner, I.V. Tsvetkova, V.A. Kurnaev, V. Bobkov, C.C. Klepper, A. Lasa, C. Guillemaut, P. Jacquet, M.F. Stamp, C. Giroud, S. Silburn, I. Balboa, E. Solano, and JET Contributors. An analytical expression for ion velocities at the wall including the sheath electric field and surface biasing for erosion modeling at jet ilw. *Nuclear Materials and Energy*, Proceedings of the 22nd International Conference on Plasma-Surface Interactions in Controlled Fusion Devices, 2016. submitted.

[23] E. Safi, G. Valles, A. Lasa, and K. Nordlund. Multi-scale modelling to relate beryllium surface

temperature, deuterium concentration and erosion behaviour in fusion reactors. *Journal of Physics D: Applied Physics*, Special Issue on Achieving Atomistic Control in Plasma-Material Interactions, 2017. Submitted.

[24] A Loarte. Understanding the edge physics of divertor experiments by comparison of 2D edge code calculations and experimental measurements. *JOURNAL OF NUCLEAR MATERIALS*, 241:118–134, 1997. 12th International Conference on Plasma-Surface Interactions in Controlled Fusion Devices, ST RAPHAEL, FRANCE, MAY 20-24, 1996.

[25] P.C. Stangeby and J.A. Tagle and S.K. Erekts and C. Lowr. Measurements of the cross-field diffusion coefficient $D_\perp$ in the edge plasma of JET. *Plasma Physics and Controlled Fusion*, 30:1787–1803, 1988.

[26] P C Stangeby, S K Erents, L de Kock, and J A Tagle. Cross-field diffusion coefficients measured in the jet edge for constant plasma current. *Plasma Physics and Controlled Fusion*, 32(6):475, 1990.

[27] R. Ding, R.A. Pitts, D. Borodin, S. Carpentier, F. Ding, X.Z. Gong, H.Y. Guo, A. Kirschner, M. Kocan, J.G. Li, G.-N. Luo, H.M. Mao, J.P. Qian, P.C. Stangeby, W.R. Wampler, H.Q. Wang, and W.Z. Wang. Material migration studies with an iter first wall panel proxy on east. *Nuclear Fusion*, 55(2):023013, 2015.

[28] A. Hakola and M.I. Airila and N. Mellet and M. Groth and J. Karhunen and T. Kurki-Suonio and T. Makkonen and H. Sillanp and G. Meisl and M. Oberkofler. ERO and PIC simulations of gross and net erosion of tungsten in the outer strike-point region of ASDEX Upgrade. *Nuclear Materials and Energy*, 2016.

[29] R. Ding, P.C. Stangeby, D.L. Rudakov, J.D. Elder, D. Tskhakaya, W.R. Wampler, A. Kirschner, A.G. McLean, H.Y. Guo, V.S. Chan, and P.B. Snyder. Simulation of gross and net erosion of high- z materials in the diii-d divertor. *Nuclear Fusion*, 56(1):016021, 2016.

[30] M. Firdaouss and V. Riccardo and V. Martin and G. Arnoux and C. Reux. Modelling of power deposition on the JET ITER like wall using the code PFCFLux . *Journal of Nuclear Materials*, 438, Supplement:S536 – S539, 2013. Proceedings of the 20th International Conference on Plasma-Surface Interactions in Controlled Fusion Devices.

[31] J. Romazanov, D. Borodin, A. Kirschner, M. Firdaouss, A. Lasa, D. Brommelö, B. Steinbusch, P. Gibbon, S. Brezinsek, Ch. Linsmeier, and JET Contributors. First application of the massively-parallel monte carlo code ero2.0 for plasma-wall interaction and 3d local impurity transport at jet ilw. *Europhysics Conference Abstracts*, 40, 2016. Proceedings of the 43rdEuropean Physical Society.

[32] Peter C Stangeby. The Scrape-Off Layer, SOL. In Peter Stott and Hans Wilhelmsson, editor, *The Plasma Boundary of Magnetic Fusion Devices*, pages 15–19. IoP, The Institute of Physics, London, 2007.

[33] N Mellet, J P Gunn, B Pgouri, Y Marandet, C Martin, and P Roubin. Tungsten erosion by impurities and redeposition: focus on the magnetised sheath. *Plasma Physics and Controlled Fusion*, 59(3):035006, 2017.

[34] P.C. Stangeby. The chodura sheath for angles of a few degrees between the magnetic field and the surface of divertor targets and limiters. *Nuclear Fusion*, 52(8):083012, 2012.

[35] Peter C Stangeby. Potential Drop in the Sheath for Floating or Biased Surfaces. In Peter Stott and Hans Wilhelmsson, editor, *The Plasma Boundary of Magnetic Fusion Devices*, pages 79–84. IoP, The Institute of Physics, London, 2007.

[36] C Björkas, D Borodin, A Kirschner, R K Janev, D Nishijima, R Doerner, and K Nordlund. Molecules can be sputtered also from pure metals: sputtering of beryllium hydride by fusion plasma-wall interactions. *Plasma Physics and Controlled Fusion*, 55(7):074004, 2013.

[37] K. Nordlund, E. Salonen, A. V. Krasheninnikov, and J. Keinonen. Swift chemical sputtering of covalently bonded materials. *Pure and Applied Chemistry*, 78(6):1203–1212, 2006.

[38] K. Nordlund, C. Björkas, K. Vörtler, A. Meinander, A. Lasa, M. Mehine, and A. V.

Krasheninnikov. Mechanism of swift chemical sputtering: comparison of be/c/w dimer bond breaking. *Nucl. Instr. Meth. Phys. Res. B*, 269(11):1257–1261, 2011.

[39] A. Lasa, K. Heinola, and K. Nordlund. Effect of beryllium on the deuterium implantation in tungsten by atomistic simulations. *Nuclear Fusion*, 2014. accepted for publication.

[40] E. Safi and C. Björkas and A. Lasa and K. Nordlund and I. Sukuba and M. Probst. Atomistic simulations of the effect of reactor-relevant parameters on be sputtering . *Journal of Nuclear Materials* , 463:805 – 809, 2015. Proceedings of the 21st International Conference on Plasma-Surface Interactions in Controlled Fusion Devices.

[41] C Björkas, K Vörtler, K Nordlund, D Nishijima, and R Doerner. Chemical sputtering of be due to d bombardment. *New Journal of Physics*, 11(12):123017, 2009.

[42] Jonathan Jacquot. *Self-consistent non-linear description of radio-frequency wave propagation and of the edge of a magnetized plasma*. PhD thesis, Universite de Lorraine, 2013.

[43] J.M Canik. Presented at APS-DPP 2016, October 31 - November 4, in San Jose, CA.

[44] M.I. Airila and C. Björkas and A. Lasa and A. Meinander and K. Nordlund and K. Vörtler. Sputtering of Be/C/W compounds in molecular dynamics and ERO simulations . *Journal of Nuclear Materials*, 438, Supplement:S589 – S593, 2013. Proceedings of the 20th International Conference on Plasma-Surface Interactions in Controlled Fusion Devices.

[45] Martin Greenwald. Verification and validation for magnetic fusion. *PHYSICS OF PLASMAS*, 17(5), MAY 2010. 51st Annual Meeting of the Division-of-Plasma-Physics of the American-Physics-Society, Atlanta, GA, NOV 02-06, 2009.

[46] Todd A. Oliver, Gabriel Terejanu, Christopher S. Simmons, and Robert D. Moser. Validating predictions of unobserved quantities. *COMPUTER METHODS IN APPLIED MECHANICS AND ENGINEERING*, 283:1310–1335, JAN 1 2015.

[47] C.C Klepper and E. Delabie. Private communication. Experiments run during M15-11 session, to be published.